

**SUMMARY**

With the help of finite-difference acoustic wave equation modeling and scale-model analysis, we study the kinematic and dynamic characteristics of strong scattering from inclusions with small radii of curvature compared to a wavelength. For an inclusion with a smooth (relative to a wavelength) curved surface, both grazing-incident and critically-incident elastic waves excite creeping waves that propagate along the inclusion surface. These results are used to formulate an elastic ray-tracing method that can be used to describe scattered waves from inclusions whose size is close to a wavelength. For all inclusion geometries modeled, including irregular inclusions, we discovered a large-amplitude arrival that was not predicted by traditional ray-theory. The raypath and traveltime of this arrival, which we term an inclusion wave, can be predicted by our ray theory.

**LIMITATION OF EXISTING THEORIES**

It is difficult to obtain analytic solutions for scatterers that have complex geometries. Even in homogeneous elastic material, the boundary conditions on the surface of a crack can make solutions to the elastic wave equation difficult to obtain. To simplify the problem of scattering, some investigators have proposed ray theories. An extension to classical geometrical ray methods was introduced by Keller (1962) in his Geometrical Theory of Diffraction (GTD). The basic idea of GTD is that an incident ray generates a cone of diffracted rays when the boundary of the inclusion is curved. The GTD has been widely used in electromagnetic and sonic wave diffraction since 1957. The GTD was extended by Achenbach et. al. (1983), who proposed that two cones of P and S diffracted rays are generated when a ray carrying a high-frequency body-wave strikes the edge of a crack. Both theories breaks down in the shadow zone of inclusion and at caustics (Achenbach et. al., 1983; Marston, 1990). One of the arrivals created by a strong scatterer that is not predicted by existing ray theory is the so-called creeping wave. The creeping wave has been shown in physical modeling to travel along the inclusion interface at the wave speed of the outer medium and take-off tangentially from the inclusion surface to the receivers.

In summary, there is currently no ray theory that reconciles with mathematical and scale modeling results and that can be used in the shadow zone of a strong scatterer.

**ULTRASONIC AND MATHEMATICAL MODELING****Parameters of Models**

Figure 1 shows the geometry of the scale models used to investigate scattering from inclusions. Inclusion models were built with four different radii, which ranged from 2.25 to 9 cm. For each model, we used a plexiglass plane with dimensions of 60×30×0.5 cm as the host material. We drilled holes of different radii for the inclusion, and finally we filled the inclusions with wax or air. For intact plexiglass, the P-wave velocity was found to be 2331 m/s, and the S-wave velocity was 1405 m/s. We used a piezoelectric transducer ( $r = 1$  cm) as the source and the receiver. The source emitted a pulse with a center frequency of 36 kHz. Consequently the wavelength was 6.5 cm and the corresponding  $ka$  for each inclusion was 2, 4, 6.5 and 9 respectively, where  $k$  is the wavenumber and  $a$  is the radius of inclusion.

Our source and receiver were assumed to have a far-field radiation pattern with the mathematics given by White (1983). For plexiglass the maximum amplitude of the compressional wave is concentrated along the axis of the transducer and the maximum amplitude of the shear wave is concentrated at an angle of 38 degree with the axis of the transducer (see Figure 1). It was important to correct for these radiation patterns in computing the amplitude scattering response of the inclusion.

From the scale-model seismograms alone, it was often difficult to correctly identify the travelpath for a specific arrival. Therefore along with traveltime and moveout analysis, we used  $f$ - $d$  acoustic wavefield snapshots to identify scattered travelpaths and wavefronts. Although the acoustic modeling did not incorporate shear and converted wave modes, and therefore did not accurately predict the scale model seismograms, wavefield snapshots were found to be invaluable in understanding the mechanics of scattering.

Wavefront snapshots for a low velocity inclusion are shown in Figure 2. These snapshots are from the same scatterer size and the same source and receiver geometry as was used in the scale-model study. Using snapshots allowed us to identify a diffracted P-wave moving around the inclusion demonstrating the creeping wave. From Figure 2 we see that the creeping wave travels along the inclusion at the outer P-wave velocity, consistent with the results of previous investigators.

**Scattering from Inclusions**

Before examining the seismograms recorded from the scale-model, we present a diagram (Figure 3) illustrating some of the wavefronts observed in the seismograms. These wavefronts display the wave

motion around and inside the inclusion due to reflection, diffraction and refraction. Further references to arrival types will correspond to the wavefront diagram in Figure 3. Figure 4 shows common shot data recorded from the circular inclusion scale-model experiment. In Figure 4a, which correspond to  $r = 2.25$  cm, the expected time-delay for P and S waves traveling around the inclusion is not obvious because the wavelength of the P-wave is nearly 3-times the inclusion radius. However, we can see two sets of diffracted P-S waves (see Figure 3) between the arrivals times of the direct P and S waves. The feature of the diffracted P-S waves in Figure 4a is similar to the data acquired from the crack models since this inclusion is quite small. The diffracted S-P wave at  $t = 210$   $\mu$ s and  $x = -4$  to  $4$  cm arrives only a few microseconds before the direct S-wave.

As the radius of the inclusion increases (Figure 4b), we see a distinct time-delay for diffracted P and S waves traveling around the inclusion. Typical kinematic traits of scattering waves emerge in Figure 4b, where the shear wave motion is dominant in the shadow zones and the compressional wave motion only appears in a small range of offsets away from the shadow zone. From  $x = -20$  to  $-12$  cm and  $12$  to  $20$  cm, and  $t = 240$  to  $320$   $\mu$ s, there are some reflected shear waves generated on the side-face of the inclusion. The analogous reflected P waves also occur faintly behind the diffracted P wave. As the inclusion radius increases to  $6.75$  cm, we saw earlier arrivals interpreted as S-P-S and S-P waves.

To compute the contribution of the scattered field to the total received energy, we calculated a coefficient of scattering shown in Figure 5. This coefficient was computed for the inclusion of radius of  $4.5$  cm. The  $y$  axis represents the amplitude ratio of different transmitted and scattered arrivals to the theoretical radiation pattern of the source and receiver. For the transmitted P and S waves, this ratio is  $A/U_r^2$  or  $A/U_s^2$ . For the converted waves the ratio is  $A/U_r U_\phi$ . For the air models, we found that over 90% of the recorded energy moved around the inclusion. Note that in the shadow zone, the energy sum of all scattered arrivals arriving as shear waves, including diffracted S, S reflection, P-S and S-P-S, exceeds that of the scattered arrivals arriving as P-waves. The energy of scattered S waves is about 60% of the total received energy in the shadow zone. This result explains why the diffracted P wave attenuates dramatically in the shadow region and how the energy is redistributed. This figure also explains why Keller's acoustic ray theory is not applicable to scattering in rocks.

### A RAY METHOD FOR DESCRIBING STRONG SCATTERING

Traditional geometrical ray theory provides an asymptotic "high frequency" approximation to wave propagation problems in a medium with locally planar interfaces. In this situation, both reflected and refracted ray obeys Snell's law. When the dimensions

of an inclusion are comparable to a wavelength, ray theory is thought to be inaccurate (Pierce and Thurston, 1992).

We propose a new ray theory that appears to accurately predict the traveltimes of all body waves scattered from an inclusion. We simplify the problem of computing the raypaths by making the following assumptions for travelpaths along inclusion boundaries, which were made by examining with the physical and  $f$ - $d$  modeling results:

(1) The critically incident point and grazing incident point divide the curved inclusion surface into three segments. The first segment is pre-critical incidence, the second is post-critical to grazing, the third is post-grazing.

(2) Both a critically-incident ray and a grazing ray excite creeping rays.

(3) The mode of creeping ray excited by critical incidence is converted.

(4) Creeping rays are geometrically equivalent to grazing incident rays.

With these constraints on rays traveling along the boundary of the inclusion, we use Snell's law to describes all raypaths:

$$V_i \cos \phi_i = V_j \cos \phi_j$$

Here  $\phi_i$  is angle between the incident ray and the inclusion tangent,  $\phi_j$  is angle between the transmitted rays and the inclusion tangent,  $V_i$  is the velocity of incident rays and  $V_j$  is velocity of transmitted rays that reflect and diffract off the inclusion or refract into the inclusion.

To verify the accuracy of our ray method, we computed ray-theoretical traveltimes for the  $r = 4.5$  cm void model. Figure 6 compares of the time-distance curves (solid line) computed using our raytrace method with time picks (black triangle) with the scale-model data of Figure 4b. From Figure 6, we can see that the most of the traveltimes are nearly identical.

However, from  $x = -8$  to  $8$  cm and  $t = 150$  -  $180$   $\mu$ s, there is some mismatch because it is difficult to identify the first-arrival of the P-S and diffracted P wave, as these arrivals interfere with each other. From the close traveltime agreement in Figure 6, we conclude that raytracing can be used to describe arrival types and times for an inclusion with a curved smooth surface (relative to wavelength), regardless of the inclusion size. We have not yet examined whether an extension to Zoeppritz equations could be used to also predict the amplitudes.

### INCLUSION WAVE

In both the  $f$ - $d$  and scale modeling with a wax inclusion, we detected a large arrival that was produced even when the inclusion was asymmetric and irregular. We term this arrival an inclusion wave, as it is not predicted by traditional ray theory. The inclusion wave is related to a ray caustic, that is two or more raypaths from an incident wave

intersecting. The wavefield snapshots in Figure 2 were used to understand the kinematic characteristics of the inclusion wave in a low velocity inclusion. On the post-grazing segment of the inclusion surface, the rays intersecting to form the caustic are produced by the creeping P-wave. As the velocity of host medium is larger than velocity in the inclusion, the wavefront formed inside inclusion is concave. After a period of time, this wavefront coils to a focussing point (the caustic). Then this point becomes a convex wavefront as it moves to the back edge of inclusion. This wavefront refracts and reflects on both sides of the inclusion surface. Inside the inclusion, more inclusion waves are generated by multiple reflection.

We also computed an irregular inclusion model. The wavefield snapshot showed that when the radii of irregular inclusion is close to wavelength, the inclusion wave still can be produced. In the range of  $1 < ka < 20$ , the inclusion wave has strong energy, because the low frequency waves have a large constructive interference zone. By incorporating caustics into our ray method, we should be able to accurately predict the traveltime of the inclusion wave. However, neither the amplitude nor the frequency dependence of the inclusion wave can be described by ray methods.

## CONCLUSIONS

We obtained the several results from ultrasonic and mathematical modeling for the inclusion models in the range of  $1 < ka < 10$ .

(1) The scattered wavefield from an inclusion with a curved surface can be described by reflected, diffracted and refracted rays. All the diffracted waves come from grazing and critical incidence. When the inclusion has a large velocity contrast with the outer medium, the refracted waves that penetrate into the inclusion consist of a relatively independent local caustic system.

(2) For receivers in the shadow zone of the scatterer, the shear component has stronger energy than the compressional component. This result suggests that any inversion technique that does not incorporate scattered shear waves will have severe limitations.

(3) A large arrival related to a ray caustic was observed in  $f-d$  and ultrasonic modeling. We term this arrival an inclusion wave since it is not predicted by traditional ray theory. In the range of  $1 < ka < 20$ , the inclusion waves can have strong energy.

By assuming that the grazing and critical incident rays excite creeping rays and that all creeping rays are geometrically equivalent to grazing incident rays, we obtained a ray method that can accurately predict arrival times for all elastic arrivals scattered from an inclusion, including the shadow region. Ray theory can be used to accurately predict all scattered arrival times for smooth inclusion with  $ka > 1$ . Interestingly, Marion and Coudin (1993) showed that ray theory could be used to accurately estimate normal

incidence direct arrival times through layered media up to  $1/d = 10$ , where  $d$  is the thickness of the layer. Our results appear to be valid up to  $1/a = 5$ . We suggest that correctly formulated ray methods can be used for seismic modeling and inversion in a wider range of applications than previously believed.

## REFERENCES

- Achenbach, J. D., Gautesen, A. K., and McMaken, H., 1982 Ray methods for waves in elastic solid: With application to scattering by cracks: Pitman Advanced Publishing Program, Boston.
- Keller, J. B., 1962, Geometrical theory of diffraction: J. Opt. Soc. Am. 52, 116-130.
- Marion, D. P., and Coudin P., 1993, From ray effective medium theories in stratified media: an experiment study: 63rd Ann. Internat. Mtg., Soc. Explo. Geophys, Expanded Abstracts. 1341-1343.
- Marston, P. L., 1992, Geometrical and catastrophe optics methods in scattering, in pierce, A. D., and Thurston, R. N., Ed(s), High frequency and pulse scattering: Academic Press Inc., 2-221.
- Pierce, A. D., and Thurston, R. N., 1992, Preface: in Pierce, A. D., and Thurston, R. N., Ed(s), High Frequency and pulse scattering: Academic Press Inc.
- White, J. E., 1983, Underground sound, Application of seismic waves: Elsevier Science Publishers B.V.

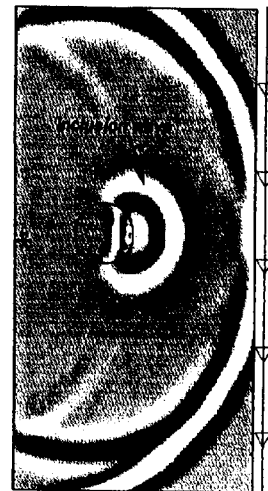
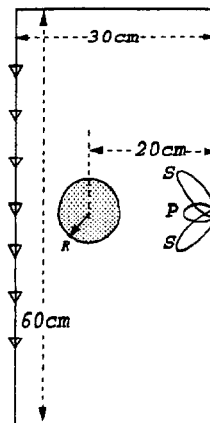


Fig. 1. The geometry of the inclusion model. The radii of inclusion respectively are 2.25, 4.5, 6.75 and 9 cm, which correspond to  $ka = 2, 4, 6.5$  and 9.

Fig. 2.  $f-d$  snapshot at 159 ms from the low velocity inclusion model. The P velocity of the outer medium is 2331 m/s and the P velocity inside the inclusion is 1500 m/s.

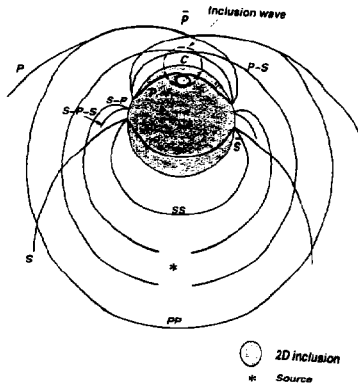


Fig. 3. The wavefronts from a low velocity scatterer. There are reflected, diffracted and refracted waves in this scattered wavefield.

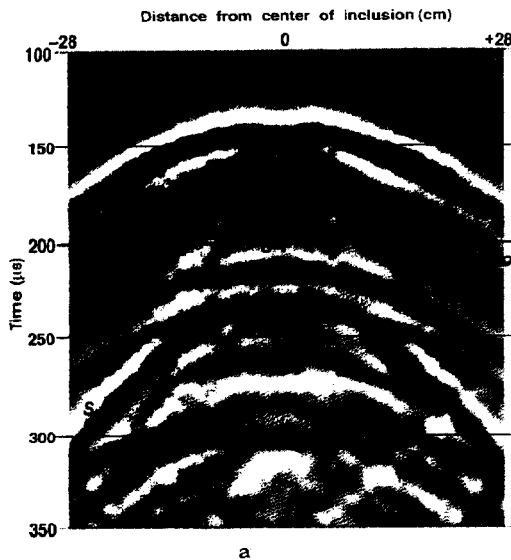


Fig. 4. Common source gray-scale seismograms from the circular inclusion scale-model with arrivals labeled. The inclusion models have different radii of (a) 2.25 cm, (b) 4.5 cm. S, P diffracted S and P waves, S-P, P-S and S-P-S converted diffracted waves are labeled. The SS arrival is a reflected wave from the side-face of the inclusion.

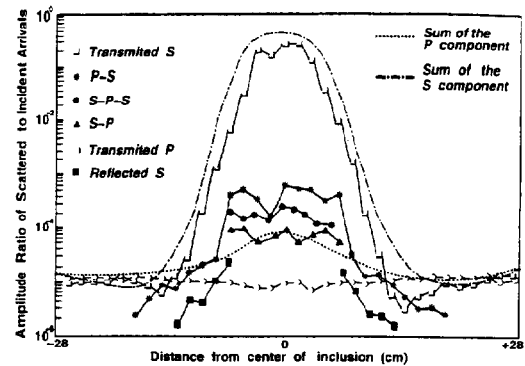
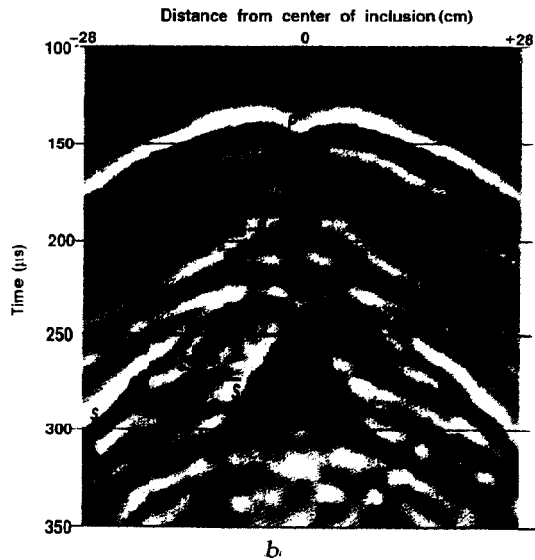


Fig. 5. Energy distribution of various scattered waves. The y axis represent the amplitude ratio of transmitted P, S to  $U_r^2, U_\phi^2$ ; and the amplitude ratio of P-S, S-P, S-P-S to  $U_r U_\phi$ ,  $U_r$  and  $U_\phi$  are computed from White's source equations.

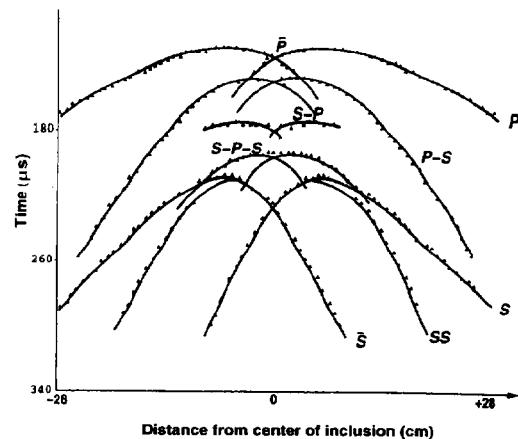


Fig. 6. Comparison between the time-distance curve (solid line) computed using our raytrace method with time picks (black triangle) from the scale-model data. The times were picked from wiggle trace displays rather than the gray-scale diagram shown in Fig. 4.



